



Provided by the author(s) and University of Galway in accordance with publisher policies. Please cite the published version when available.

Title	Influence of material inhomogeneity on the mechanical response of a tempered martensite steel
Author(s)	Li, Ming; Sun, F. W.; Barrett, Richard A.; Meade, E.; Li, D. F.; O'Donoghue, Padraic E.; Leen, Sean B.; O'Dowd, Noel P.
Publication Date	2017-01-13
Publication Information	Li, M., Sun, F., Barrett, R., Meade, E., Li, D., O'Donoghue, P., ... O'Dowd, N. (2017). Influence of material inhomogeneity on the mechanical response of a tempered martensite steel. Proceedings of the Institution of Mechanical Engineers, Part L: Journal of Materials: Design and Applications, 231(1-2), 14-22. https://doi.org/10.1177/1464420716687785 Copy to Clipboard
Publisher	SAGE Publications
Link to publisher's version	https://doi.org/10.1177/1464420716687785
Item record	http://hdl.handle.net/10379/15645
DOI	http://dx.doi.org/10.1177/1464420716687785

Downloaded 2024-04-19T10:38:18Z

Some rights reserved. For more information, please see the item record link above.



Influence of Material Inhomogeneity on the Mechanical Response of a Tempered Martensite Steel

M. Li^{1,2}, F.W. Sun², R.A. Barrett¹, E. Meade², D.F. Li³, P.E. O'Donoghue¹, S.B. Leen¹,
N.P. O'Dowd²

¹National University of Ireland Galway, Galway, H91 HX31, Ireland

²Bernal Institute, School of Engineering, University of Limerick, Limerick, V94 T9PX, Ireland

³Shenzhen Graduate School, Harbin Institute of Technology, Shenzhen 518055, China

Abstract: Failure in steel weldments operating at high temperatures often occurs in the heat affected zone (HAZ) adjacent to the weld. Such failures can be a result of material inhomogeneity within the HAZ and in the case of tempered martensite steels has been linked with regions of untransformed α (ferrite) phase or over-tempered martensite within the intercritical region of the HAZ (IC-HAZ). In this work, two-dimensional Voronoi tessellation is used to construct polygonal Voronoi cells to represent the microstructure of the HAZ of a weld in a tempered martensite steel. The Voronoi construction is treated as a representative volume element (RVE) of the material and is discretized by 8-node linear brick elements, with periodic boundary conditions. The lattice orientation at each material point is specified by three Euler angles, which are assumed to be randomly distributed, to represent the initial lack of texture in the IC-HAZ. The constitutive response is represented by a nonlinear, rate-dependent, finite-strain crystal plasticity model. The results indicate that small amounts of ferrite can induce significant enhancements in stress and inelastic deformation at the interface of the ferrite and martensite grains. This localisation of stress and strain may be critical for microcrack and/or void formation and may be a contributory factor to Type IV cracking.

Keywords: *weldment, microstructure modelling, crystal plasticity, tempered martensite, IC-HAZ*

1. Introduction

Tempered martensite ferritic steels, such as modified 9Cr-1Mo steels, are widely used in steam pipework systems of conventional power plants, designed to endure long-term loading at elevated temperatures [1]. Many of the failures of such components occur at welded connections due to the occurrence of weld defects and the existence of microstructure gradients following welding [2-3]. Such microstructure gradients occur due to the different thermal conditions experienced by the material during welding, both in the weld material and in the HAZ adjacent to the weld (see Figure 1). The degree of microstructure change depends on the maximum heat exposure and the cooling rate, both of which are dependent on the distance from the weld fusion line, as illustrated in Figure 1. Typically the HAZ consists of a coarse grain heat affected zone (CG-HAZ), closest to the weld, where the peak temperature is much higher than A_{c3} (the temperature at which transformation of ferrite, α , to austenite, γ , is complete during heating) but below the solid-liquid transition temperature, a fine grain heat affected zone (FG-HAZ) where the peak temperature is above A_{c3} , and an inter-critical heat affected zone (IC-HAZ), adjacent to the parent metal where the peak temperature during welding is between A_{c1} (the temperature at which austenite begins to form during heating) and A_{c3} . This IC-HAZ region may include ferrite and martensite phases due to the transformation of the austenite grains to martensite during rapid cooling [4-7] and is of particular importance for welded connections which fail in the IC-HAZ, a phenomenon known as Type-IV cracking [1-9]. The IC-HAZ can be considered to be a type of dual-phase material with a relatively high strength, low ductility martensite phase and a low volume

fraction of lower strength, high ductility ferrite phase [10]. It has been reported that the microstructure of dual-phase steels, e.g. grain size, volume fraction, phase distribution, martensite morphology, carbon content, can have an important influence on the overall mechanical behavior (e.g. yield stress, ductility) of such dual-phase steels [11-13].

Advances in microstructural modelling of mechanical behavior of crystalline materials have opened up new opportunities for accurately estimating the structural integrity of a component [14-17]. For example, in [14] a multi-scale modelling approach was adopted to investigate the effect of precipitate and lath coarsening on the mechanical response of a martensitic steel. Such studies have often been carried out in conjunction with novel experimental approaches to quantify deformation at the microscale, e.g. micro-pillar tests to determine the constitutive behaviour and over-all response in dual phase steels [18-19]. Currently, there are two predominant explanations to account for the premature failure of weldments and the associated Type IV cracking. One attributes the weakness in the weldment to the low strength of the IC-HAZ [4-6,20] and the other attributes it to microstructural gradients leading to different deformation and stress states in each region [7,21]. The former could be considered a material-based explanation and the latter a mechanics-based one. In reality, the material and the mechanics are closely coupled as we demonstrate in this work. Here, we build on our previous studies on engineering steels [16,22-24] to investigate the influence of a soft ferrite phase within a hard martensitic region, representing the IC-HAZ of a modified 9Cr-1Mo tempered martensite steel such as ASTM A335/ASME SA335 P91. A RVE of a collection of grains with random crystal orientation is constructed using Voronoi Tessellation [25] and the finite-element method is used to determine the resultant stress and strain distribution within the RVE. A crystal plasticity model is used to capture the deformation characteristics of both phases of the IC-HAZ.

2. Crystal plasticity model

A standard approach [26] is adopted to represent the kinematics of deformation with an overall deformation gradient, \mathbf{F} , which is decomposed as follows:

$$\mathbf{F} = \mathbf{F}^e \mathbf{F}^p, \quad (1)$$

where \mathbf{F}^e is the elastic deformation gradient, incorporating elastic stretching and rigid rotation, and \mathbf{F}^p accounts for the inelastic deformation based on slip-based plastic deformation in a crystalline material. The plastic velocity gradient, \mathbf{L}^p , is a function of the accumulated slip rates on N possible slip systems:

$$\mathbf{L}^p = \dot{\mathbf{F}}^p (\mathbf{F}^p)^{-1} = \sum_{\alpha=1}^N \dot{\gamma}^{\alpha} \mathbf{m}^{\alpha} \otimes \mathbf{n}^{\alpha}, \quad (2)$$

where $\dot{\gamma}^{\alpha}$ is the slip rate of slip system α and \mathbf{m}^{α} and \mathbf{n}^{α} are slip direction and slip plane normal vectors of the slip system α , respectively. For martensitic materials, for the martensite steel there are 48 slip systems potentially active, consisting of 12 $\langle 111 \rangle \{110\}$ slip systems, 12 $\langle 111 \rangle \{112\}$ slip systems and 24 $\langle 111 \rangle \{123\}$ slips systems [16,18]. A thermal activated flow rule is employed relating the slip rate on a slip system to the resolved shear stress on that system:

$$\dot{\gamma}^{\alpha} = \dot{\gamma}_0 \exp \left(-\frac{F}{kT} \left\langle 1 - \left\langle \frac{|\tau^{\alpha}| - S^{\alpha}}{\tau_0} \right\rangle^p \right\rangle^q \right) \quad (3)$$

Here, F is a constant related to thermal activation energy required to overcome the lattice resistance, k is the Boltzmann constant and T is absolute temperature. The constants p and q are the exponential and pre-exponential constants, respectively; τ^α and S^α are the resolved shear stress and slip resistance of slip system α , respectively, with

$$\tau^\alpha = \boldsymbol{\sigma} : \mathbf{m}^\alpha \otimes \mathbf{n}^\alpha, \quad (4)$$

$$\dot{S}^\alpha = \sum_{\beta=1}^N h^{\alpha\beta} \left(\frac{S_{sat} - S^\beta}{S_{sat} - S_0} \right) |\dot{\gamma}^\beta|, \quad (5)$$

where $\boldsymbol{\sigma}$ in Equation (4) is the stress tensor; S_{sat} in Equation (5) is the saturated value of slip resistance with an initial value of S_0 ; $h^{\alpha\beta}$ is the hardening matrix and can be written as:

$$h^{\alpha\beta} = h_s [q_0 + (1 - q_0) \delta_{\alpha\beta}] \quad (6)$$

where h_s is a material parameter, q_0 is the latent hardening factor and $\delta_{\alpha\beta}$ is the Kronecker delta. For this material, q_0 is unity [25], corresponding to Taylor hardening (all the components of the hardening matrix are identical). The material model is implemented through a user subroutine (UMAT) in a commercial finite-element code Abaqus [27].

3. Microstructure modelling

3.1 Microstructure model generation

In order to predict the localised inelastic response of the material, a representative microstructure generated using Voronoi tessellation [24,25], has been constructed including sufficient numbers of convex polygonal grains to represent the overall mechanical behaviour of the material (see Figure 2). Here each polygon represents a martensite block (or ferrite grain) with a different orientation in the polycrystalline model. (It should be noted that the martensite blocks will not generally take the shape of regular polygons—the current approach is a first step at a physical representation of the material microstructure). The two dimensional model is constructed with each block randomly assigned three Euler angles to specify the orientation of the block. A finite-element mesh is then generated using 3D elements, with one element through the thickness extruded in the normal direction (z direction in Figure 2). Grain boundaries are assumed to be perfectly bonded and no special elements are used at grain boundaries. The RVE is loaded with a uniform monotonic displacement in the y direction. Periodic boundary conditions are applied, to represent a large (infinite) collection of grains. Periodicity in the z direction corresponds to the case of columnar grains. In previous work [22,24], it has been found that under in-plane loading this pseudo-3D representation of the microstructure provides a good prediction of the stress and strain distributions when compared with a full 3D Voronoi tessellation model.

4. Results and discussion

4.1 RVE size determination

As illustrated in Figure 2, three different RVEs were constructed to investigate the sensitivity of the response to the RVE size, i.e. the number of grains in the RVE. Note that since a length-scale independent model is used in this work there is no explicit grain size effect on the result. Each RVE is loaded with a uniform monotonic displacement up to a strain of 1% at a strain rate of 0.1%/s. The resultant true strain-stress curve is shown in Figure 3. It may be seen that a converged solution is obtained when the number of grains exceeds 200. Further study on the 200-grain RVE demonstrated that for different random sets of grain orientations as measured by the three Euler angles (see Figure 4), the same response is obtained (see

Figure 5), confirming that the 200-grain RVE provides a representative response of the material.

4.2 Model calibration

The crystal plasticity material model described here has a total of 10 independent material constants. Based on the results in [21] which showed that the measured tensile response of the ICHAZ was very similar to that of the base metal P91, and assuming that the volume fraction of the ferrite phase in the ICHAZ is low [5], the response of the martensite phase of the IC-HAZ can be represented by that of the base metal. Table 1 gives the parameters of the martensite phase (IC-HAZ) at room temperature used in this work obtained by calibrating the material parameters in Eqs. 3 and 5 with the 200 grain RVE to match the measured tensile response of P91. The values of p and q in the flow rule, Eq. (3) are those suggested in [28] for a body centered-cubic (BCC) material, *viz.* $p = 0.5$ and $q = 1.25$.

It had been reported in [6,20,29] that the IC-HAZ is the region of the weldment with the lowest hardness, and in [5], it is suggested that the presence of a soft ferrite phase in the IC-HAZ could be responsible for the low hardness. Based on this assumption and on existing experimental results for dual phase steels [18,30], we assume that the lattice friction stress (τ_{0f}) of the ferrite phase (see equation 3) is lower than that of the martensite phase (τ_0). The relationship between τ_0 and τ_{0f} is described by the ratio R ,

$$R = \frac{\tau_0}{\tau_{0f}}. \quad (7)$$

$R = 1$ implies that the IC-HAZ is comprised of martensite only, $R = 2$ implies that the lattice friction stress of the ferrite phase is half that of the martensite phase. All other material constants are assumed to be the same for the two phases. The comparison of the macro stress-strain response of the two different phases, obtained from the 200-grain RVE in Figure 2, is shown in Figure 6, which also includes the experimental data for the P91 material, from [16].

4.3 Mesh sensitivity study

A mesh sensitivity study for the global and local response is described in this section. Two 200-grain models, with 35,000 elements and 62,000 elements, respectively, were generated (see Figure 7). In each case, one grain labelled ‘f’ in Figure 7, has been assigned ferrite properties ($R = 2$). The two models have the same orientation for the corresponding grains. Uniaxial loading was applied to both models up to 2% strain. As seen in Figure 8, the macroscopic stress responses are found to be indistinguishable for the two meshes. For the local response study, the local maximum principal stress and accumulated equivalent plastic strain, ε_{eq} , are examined at the ferrite grain boundary—Path 1, as illustrated in Figure 7(b). Accumulated equivalent plastic strain has been proposed by a number of authors, e.g. [31], as an important indicator parameter for crack initiation and initiation of micro-cracks under stress controlled conditions would expect to be controlled by maximum principal stress [32]. Good agreement between the two meshes is seen in Figure 9. These results indicate that the 35,000-element mesh is a converged mesh for the problem examined, and is henceforth used in this study to see the local response with the effect caused by ferrite phase. We have also investigated the influence of the location of the ferrite grain within the RVE and find that the same trends are observed.

4.4 Influence of strength of ferrite matrix

Due to the low volume fraction of ferrite [5], the influence on the macroscopic stress-strain response is negligible and attention is focused on the local response. Figure 10 depicts the

maximum principal stress and equivalent strain for different ratios of R along a path traversing the ferrite and martensite grains, designated Path 2 in Figure 10(a), at the same remote strain level (2%). As expected, stress and strain are discontinuous across the grain boundary even for $R = 1$ due to the different crystal/block orientations. The average misorientation between the ferrite grain and the neighbouring martensite grains (blocks) is 30.5° (using the crystal deformation definition in [33] to quantify mis-orientation between grains). As R increases, the peak stress at the martensite-ferrite boundary increases significantly from approx. 520 MPa to approx. 680 MPa. In all cases the peak accumulated equivalent plastic strain is in the softer ferrite grain and the peak strain increases with increasing R (decreasing strength of the ferrite grain), with the peak value increasing from approx. 3.7% for $R = 1$ to approx. 7.4% for $R = 4$. Thus, the occurrence of the soft ferrite phase within a hard martensite matrix leads to a stress concentration at the ferrite-martensite boundary matrix and higher plastic strains at the boundary and within the ferrite phase. It may be noted that similar trends have been observed in simulations of hard/soft grain combinations within titanium alloy polycrystals [17]. It has also been reported that crack-like cavities may form along the ferrite/martensite grain boundary in the ICHAZ of a P91 weld [6], indicating that these areas are locations of stress/strain concentration.

Contours of maximum principal stress, corresponding to the results in Figure 10 are provided in Figure 11, again corresponding to a remote strain of 2% in each case. The larger contour plots in Figure 11 give the result for the full 200-grain RVE while the smaller contour plots provide the results close to the ferrite grain (indicated by 'f' in the zoomed-in figures). It may be noted that even when the applied loading is uniform and $R = 1$, the local stress distribution is quite inhomogeneous inside the RVE, due to the different lattice orientations of the grains. In Figure 11(a), the increase in stress at the ferrite-martensite boundary is clear from these contours: see corresponding regions 1 and 2, indicated in the zoomed-in Figure 11(a). There is also a small increase in stress in region 3 with increasing R and a corresponding reduction in stress in the ferrite grain with increasing R . In Figure 11(b), the local increase in plastic strain with increasing R may also be noted. Away from the ferrite grain, the stress and strain distributions within the material are unaffected.

4.5 Effect of ferrite aggregation

The results of Section 4.4 are for an isolated ferrite grain. In Figure 12 results for 1, 2 and 3 ferrite grains, respectively are presented (the results for $N = 1$ from Section 4.4 are included for convenience). Significant localization of plastic deformation can be observed in Figure 12(b) as the number of ferrite grains increase. These bands of high plastic strain occur at the ferrite-martensite boundary.

5. Conclusions

This work examines an idealised microstructure of the intercritical region in the heat affected zone of a modified 9Cr-1Mo steel. The results are also applicable to other dual-phase steels with ferrite-martensite phase distributions. The results indicate that a soft ferrite phase, even at low volume fraction, can have a significant influence on local stress and strain behaviour, and hence crack initiation behaviour and material lifetimes. Such results will provide insights into optimised heat treatments for welded martensite components and material design. Future work in this area is required to obtain more quantitative information on ICHAZ microstructure and identification of ferrite-martensite phases within the HAZ. A combination of scanning and transmission electron microscopy (SEM, TEM) in conjunction with electron back scattered diffraction (EBSD) may provide complementary insights into this issue.

Acknowledgments

This publication has emanated in part from research conducted with the financial support of Science Foundation Ireland under Grant No. 14/IA/2604. The modelling work was supported by the Irish Centre for High-End Computing (ICHEC). Helpful discussions with Mr Brian Golden, Dr Yina Guo of the Bernal Institute at University of Limerick, Ireland, and Prof. Fengshi Yin of Shan Dong University of Technology, China. Mr Stephen Scully and Ms Adelina Adams of ESB Energy International (Ireland) are gratefully acknowledged.

References:

1. Farragher, T.P., Scully, S., O'Dowd, N.P., and Leen, S.B., "Thermomechanical analysis of a pressurized pipe under plant conditions," *Transactions of the ASME Journal of Pressure Vessel Technology*, **135** (2013), 011204.
2. Abe, F., Tabuchi, M., Kondo, M. and Tsukamoto, S. "Suppression of Type IV fracture and improvement of creep strength of 9Cr steel welded joints by boron addition," *International Journal of Pressure Vessels and Piping*, **84** (2007), 44-52.
3. Li, M., Barrett, R.A., Scully, S., Harrison, N.M., Leen, S.B. and O'Donoghue, P.E. "Cyclic plasticity of welded P91 material for simple and complex power plant connections," *International Journal of Fatigue*, **87**(2016), 391-404.
4. Gaffard, V., Gourgues-Lorenzon A.F. and Besson, J., "High temperature creep flow and damage properties of the weakest area of 9Cr1Mo-NbV martensitic steel weldments," *ISIJ International*, **45**(2005), 1915-1924.
5. Thomas Paul, V., Saroja, S., Hariharan, P., Rajadurai, A. and Vijayalakshmi, M., "Identification of microstructural zones and thermal cycles in a weldment of modified 9Cr-1Mo steel," *J Mater Sci*, **42**(2007), 5700-5713.
6. Lee, J.S. and Maruyama, K., "Mechanism of microstructure deterioration preceding type IV failure in weldment of Mod. 9Cr-1 Mo steel," *Met. Mater. Int.*, **4**(2015), 639-645.
7. Divya, M., Das, C.R., Albert, S.K., Goyala, S., Ganesh, P., Kaul, R., Swaminathan, J., Murtyd, B.S., Kukreja, L.M. and Bhaduria, A.K., "Influence of welding process on Type-IV cracking behaviour of P91 steel," *Materials Science & Engineering A*, **613**(2014), 148-158.
8. Hongo, H., Tabuchi, M. and Watanabe, T., "Type IV creep damage behaviour in Gr.91 steel welded joints," *Metallurgical and Materials Transactions A*, **43**(2012), 1163-1173.
9. Francis, J.A., Mazur, W. and Bhadeshia, H.K.D.H., "Type IV cracking in ferrite power plant steels," *Material Science and Technology*, **22**(2006), 1938-1995.
10. Liedl, U., Traint, S. and Werner, E.A., "An unexpected feature of the stress-strain diagram of dual-phase steel," *Computational Materials Science*, **25** (2002), 122-128.
11. Bag, A., Ray, K.K. and Dwarakagasa, E.S., "Influence of martensite content and Morphology on Tensile and impact properties of high-martensite Dual-Phase steels," *Metallurgical and Materials Transactions A*, **30**(1999), 1193-1202.
12. Kumar, A., Singh, S.B. and Ray, K.K., "Influence of bainite/martensite content on the tensile properties of low carbon dual-phase," *Material Science & Engineering (A)*, **474**(2008), 270-282.
13. Movahed, P., Kolahgar, S., Marashi, S.P.H., Pouranvarib, H. and Parvina, N., "The effect of inter-critical heat treatment temperature on the tensile properties and work hardening behaviour of ferrite-martensite dual phase steel sheets," *Material Science and Engineering A*, **518**(2009),1-6.
14. Li, D.F., Golden B.J. and O'Dowd, N.P., "Multiscale modelling of mechanical response in a martensitic steel: A micromechanical and length-scale-dependent frame work for precipitate hardening," *Acta Materialia*, **80**(2014), 445-456.

15. Busso, E.P., Meissonnier, F.T. and O'Dowd, N.P., "Gradient-dependent deformation of two-phase single crystals," *Journal of the Mechanics and Physics of Solids*, **48**(2000), 2333-2361.
16. Golden, B.J., Li, D.F., Guo, Y.N., Tiernan, P., Leen, S.B. and O'Dowd, N.P., "Microscale deformation of a tempered martensite ferritic steel: Modelling and experimental study of grain and sub-grain interactions," *Journal of the Mechanics and Physics of Solids*, **86**(2016), 42-52.
17. Dunne, F.P.E., Rugg, D. and Walker, A., "Length scale-dependent, elastically anisotropic, physically-based hcp crystal plasticity: Application to cold-dwell fatigue in Ti alloys," *International Journal of Plasticity*, **23**(2007), 1061-1083.
18. Chen, P., Ghassemi-Armaki, H., Kumar, S., Bower, A., Bhat, S. and Sadagopan, S., "Microscale-calibrated modelling of the deformation response of dual-phase steels," *Acta Materialia*, **65**(2014), 133-149.
19. Ghassenmi-Armaki, H., Maab, R., Bhat, S.P., Sriram, S., Greer, J.R. and Kumar, K.S., "Deformation response of ferrite and martensite in a dual-phase steel," *Acta Materialia*, **62**(2014), 197-211.
20. Laha, K., Chandravathi, K.S., Parameswaran, P., Bhanu Sankara Rao, K. and Mannan, S.L., "Characterization of microstructures across the Heat-Affected Zone of the Modified 9Cr-1Mo weld joint to understand its Role in Promoting Type IV Cracking," *Metallurgical and Materials Transactions A*, **38A**(2007), 58-68.
21. Touboul, M. Crepin, J. Rousselier, Latourte, G. F. and Leclercq, S., "Identification of local viscoplastic properties in P91 welds from full field measurements at room temperature and 625 °C," *Experimental Mechanics*, **53**(2013), 455-468.
22. Li, D.F. and O'Dowd, N. P. "Investigation ductile failure at the microscale in engineering steels: A micromechanical finite elements model," *ASME PVP Conference*, 2012, Toronto.
23. Golden, B.J., Li, D.F., O'Dowd, N.P. and Tiernan, P., "Microstructure modelling of P91 martensitic steel under uniaxial loading conditions," *Journal of Pressure Vessel Technology*, **136**(2014), 021404-1-021404-6.
24. Li, D.F., Davies, C.M., Zhang, S.Y., Dickinson, C. and O'Dowd, N.P., "The effect of prior deformation on subsequent micro-plasticity and damage evolution in austenitic stainless steel at elevated temperature," *Acta Materialia*, **60**(2013), 3575-3584.
25. Li, D.F. and O'Dowd, N.P., "On the evolution of lattice deformation in austenitic stainless steels: The role of work hardening at finite strains," *Journal of the Mechanics and Physics of Solids*, **59**(2011), 2421-2441.
26. Asaro, R.J. and Rice, J.R., "Strain localization in ductile single crystals," *Journal of Mechanics and Physics Solids*, **25**(1977), 309-38.
27. ABAQUS V6.11. Providence (RI): Hibbitt, Karlsson and Sorensen, 2011.
28. Weinberger, C.R., Boyce, B.L. and Battaile, C., "Slip planes in bcc transition metals," *International Materials Reviews*, **58**(2013), 196-314.
29. Vani Shankar, K., Mariappan, R. and Sandhya, R., Mathew, M. D. and Jayakumar, T., "Effect of application of short and long holds on fatigue life of Modified 9Cr-1Mo steel weld joint," *Metallurgical and Materials Transactions A*, **45A**(2014), 1390-1440.
30. Hamelin, C.J., Muransky, O., Smith, M.C., Holden, T.M., Luzina, V, Bendeicha, P.J. and Edwards, L., "Validation of a numerical model used to predict phase distribution and residual stress in ferritic steel weldments," *Acta Materialia*, **75**(2014), 1-19.
31. Sweeney, C.A., O'Brien, B., Dunne, F.P.E., McHugh, P.E. and Leen, S.B. "Strain-gradient modelling of grain size effects on fatigue of CoCr stents," *Acta Materialia*, **78** (2014), 341-353.

32. G. Fajdiga, M. Sraml, R. Piques, "Crack initiation and propagation under multiaxial fatigue," *Engineering Fracture Mechanics*, **76**(2009) 1320–1335.
33. Ralf, Hielscher, Helmut Schaeben, Heinrich Siemes, "Orientation distribution within a single hematite crystal," *Math Geosci*, **42**(2010) 359-375.
34. Xinhua Y., "Multi-Scale characterization of heat-affected zone in martensitic steels," *PhD thesis*, 2012, The Ohio State University.
35. Indacochea, J.E., Wang, G., Seshadri, R., "Creep rupture properties of high-temperature Bainitic steels after weld repair," *Journal of Engineering Material and Technology*, **122**(2000), 259-263.

Figures:

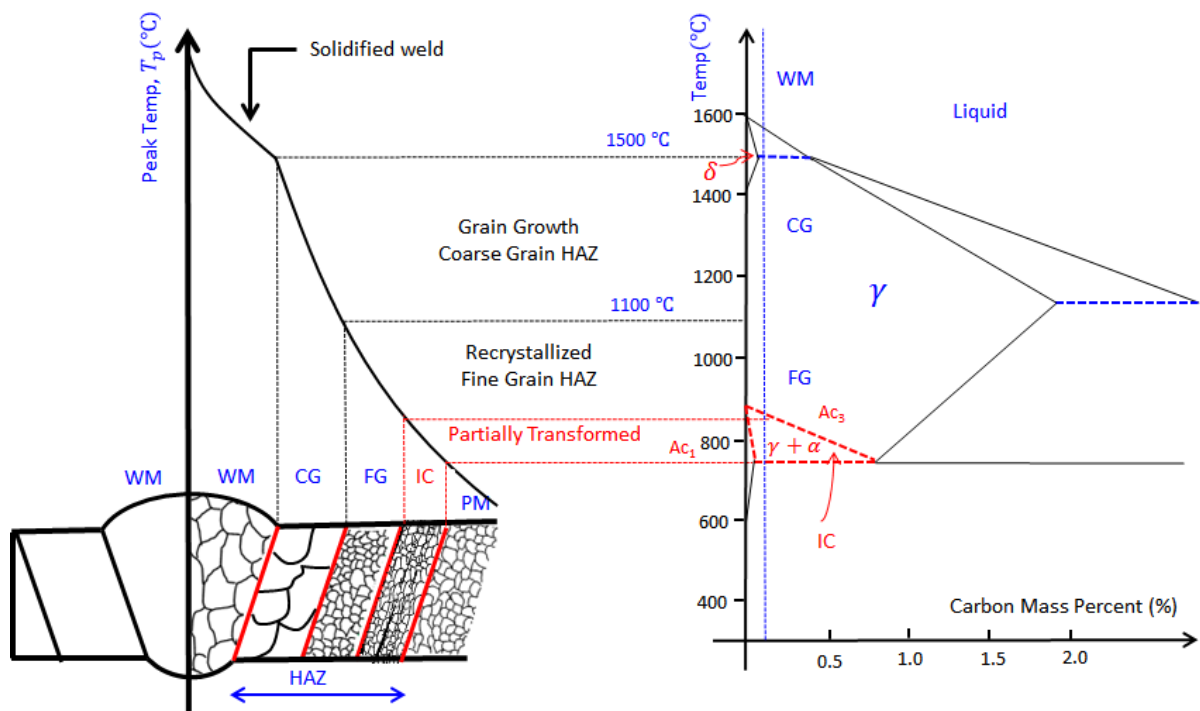


Figure 1: A schematic of the weldment regions as they correspond to the Fe-C binary phase diagram, where dash line show the carbon content of P91 [34-35]

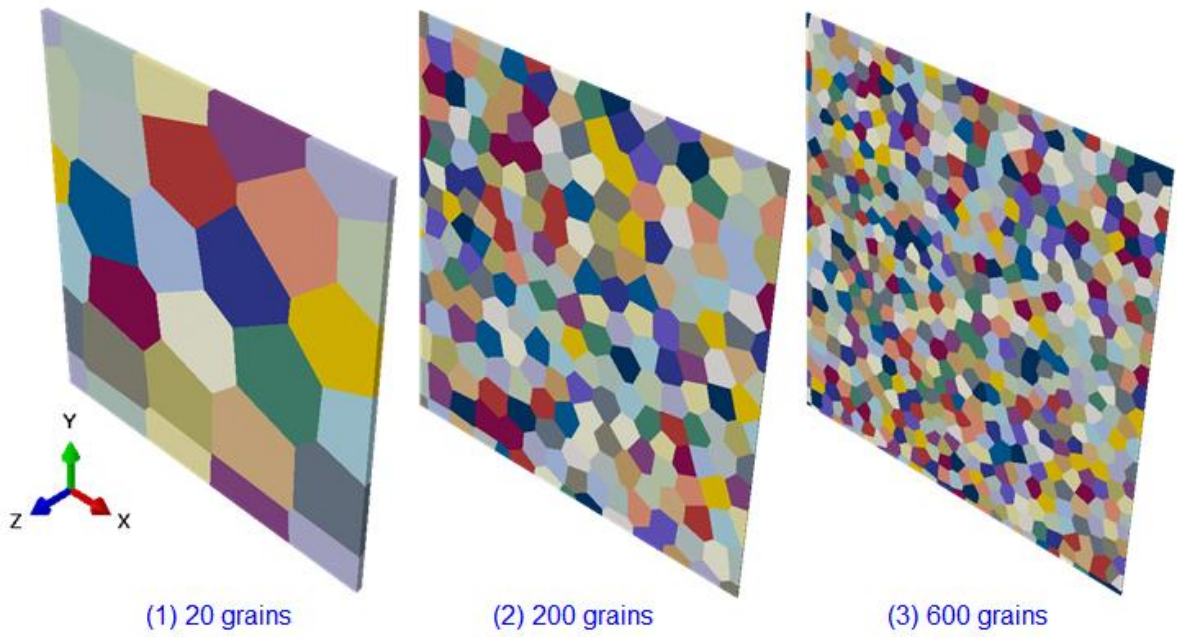


Figure 2: Three representative volume element (RVE) consisting of different numbers of grains with random orientation

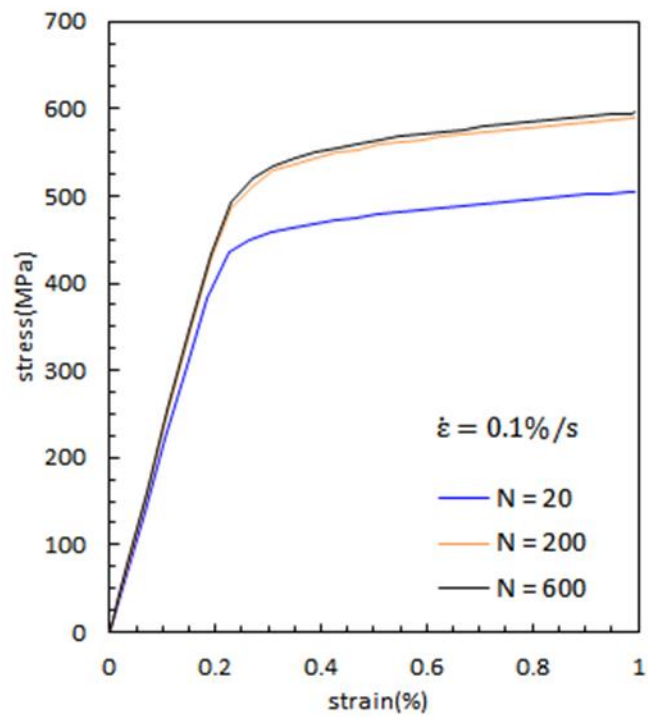


Figure 3: RVE size effect on monotonic stress–strain response (macro-response).

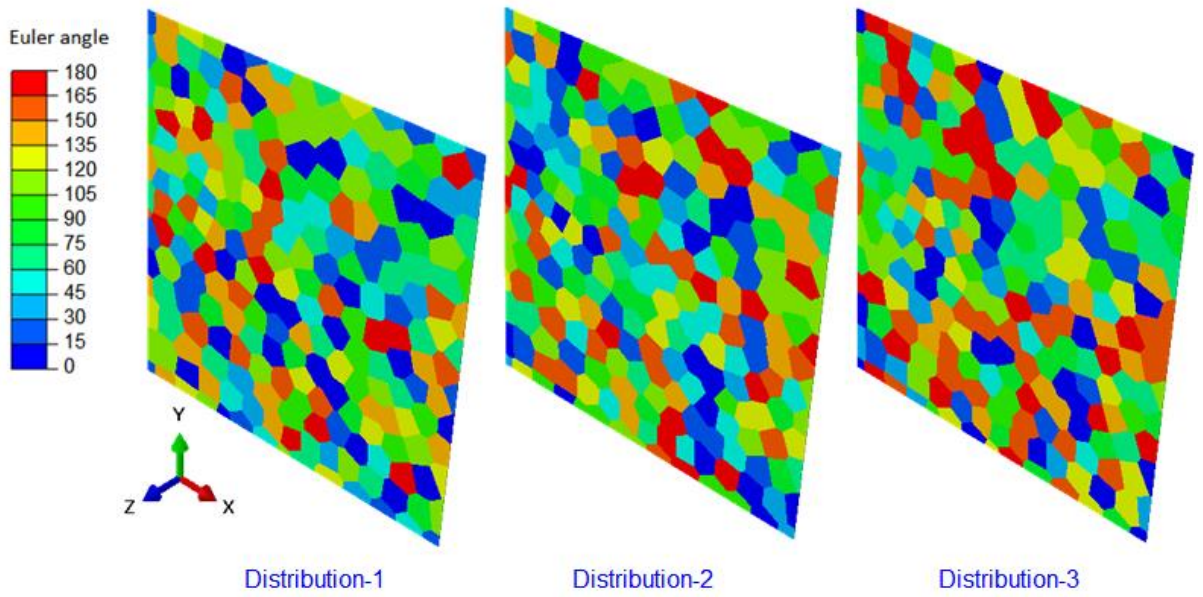


Figure 4: 200-grains RVE with three different random crystal orientations

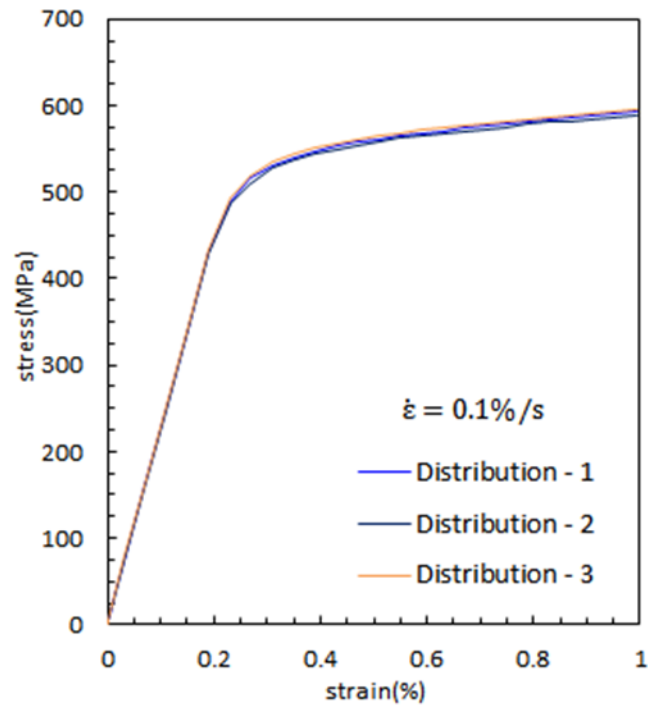


Figure 5: Effect of three different random lattice orientations on the monotonic stress–strain (macro-response) of the 200-grain RVE.

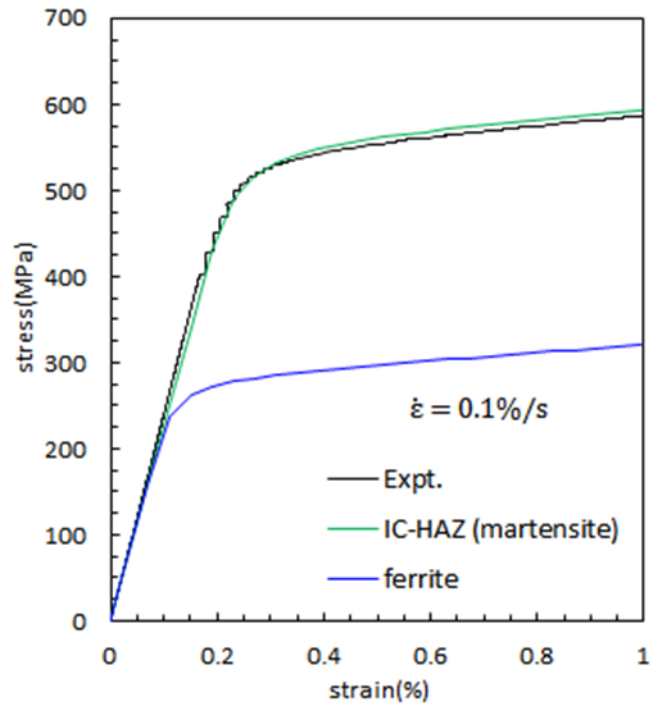


Figure 6: Comparison of IC-HAZ RVE simulation with room temperature uniaxial data for P91 [16]. Also included is the predicted response for the ferrite phase using the RVE with $R = 2$ (see Eq. 7).

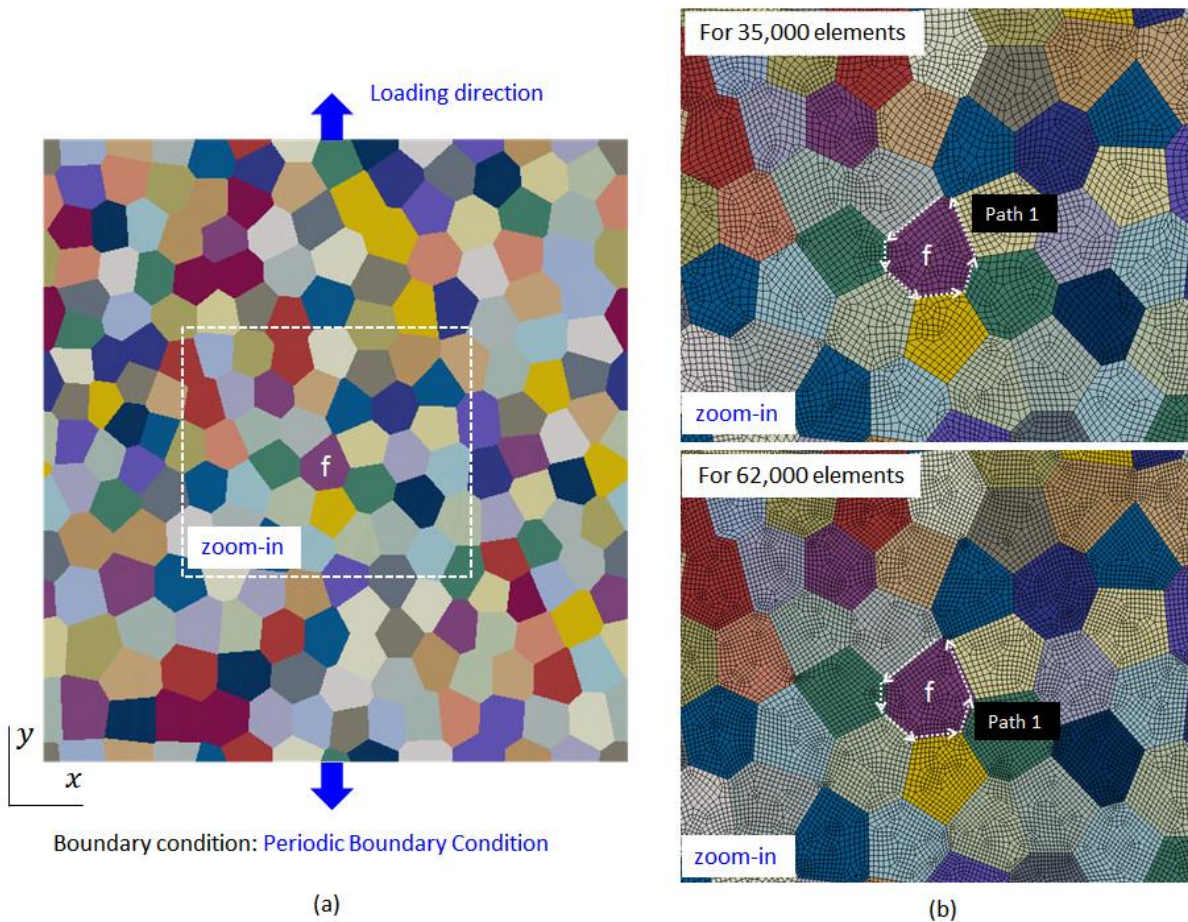


Figure 7: Illustration of mesh sensitivity study for 200-grains RVE with an isolated ferrite embedded within the martensite matrix (a) Overall mesh (b) zoomed-in mesh showing the Path1 used to plot variables outputs.

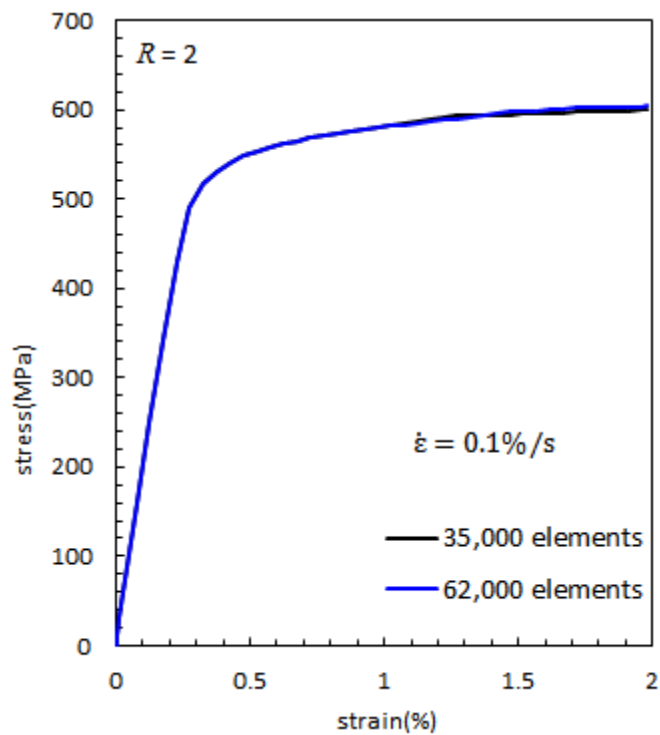
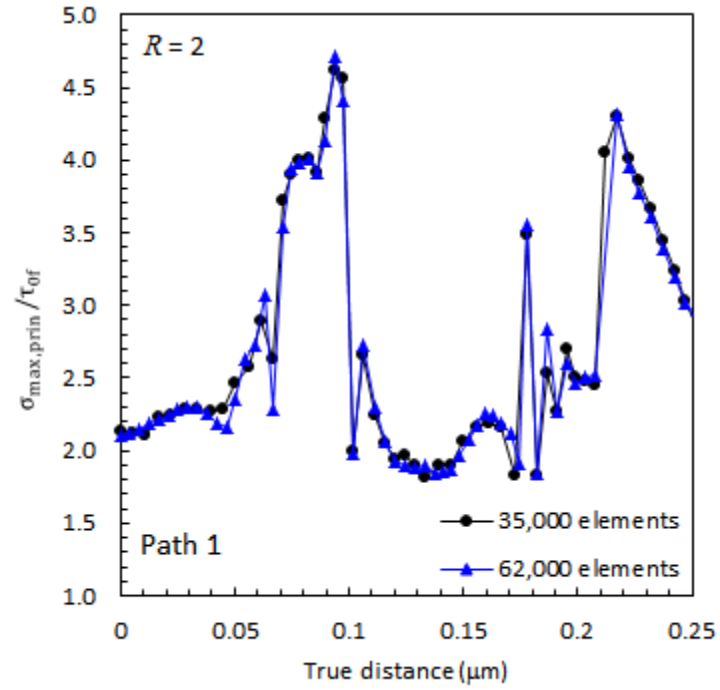


Figure 8: Macro-response of 200-grain RVE with different mesh densities

(a)



(b)

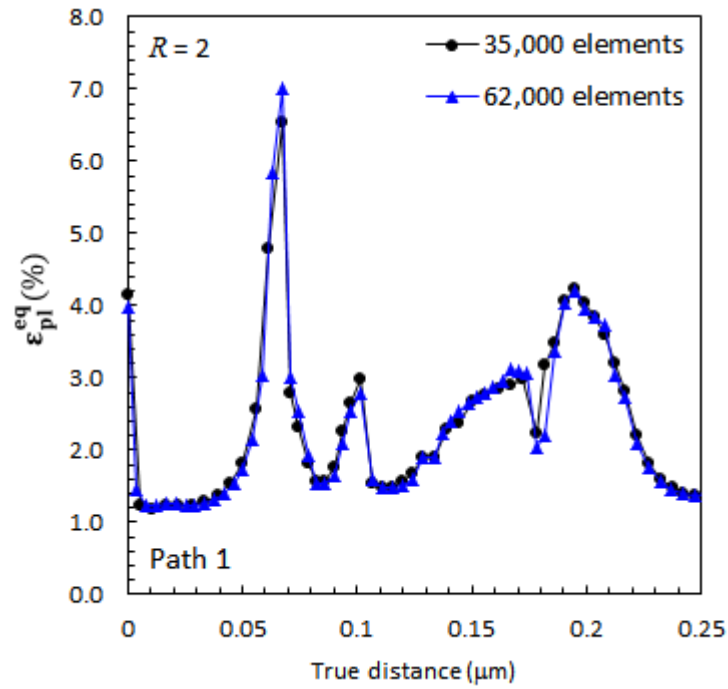
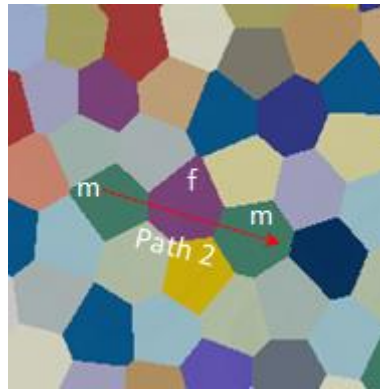
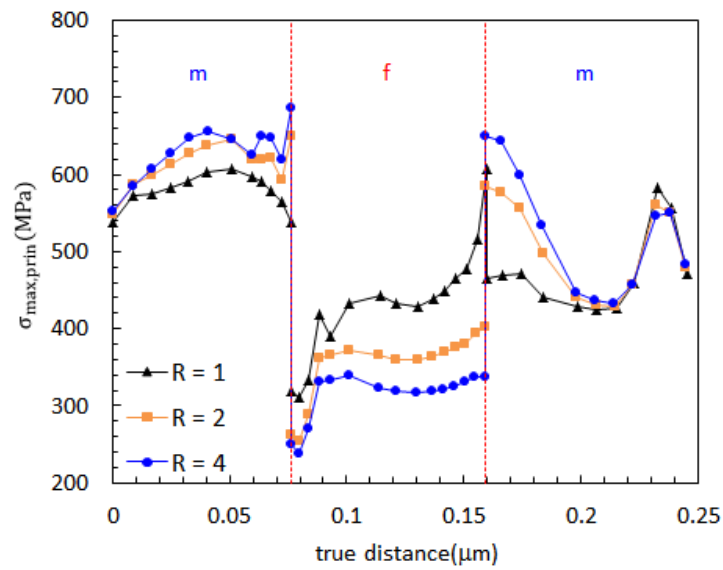


Figure 9: Distribution of local variables along the ferrite grain boundary with different mesh densities, the path had been shown in Figure 7: (a) maximum principal stress and (b) accumulated equivalent plastic strain (ϵ_{eq}).

(a)



(b)



(c)

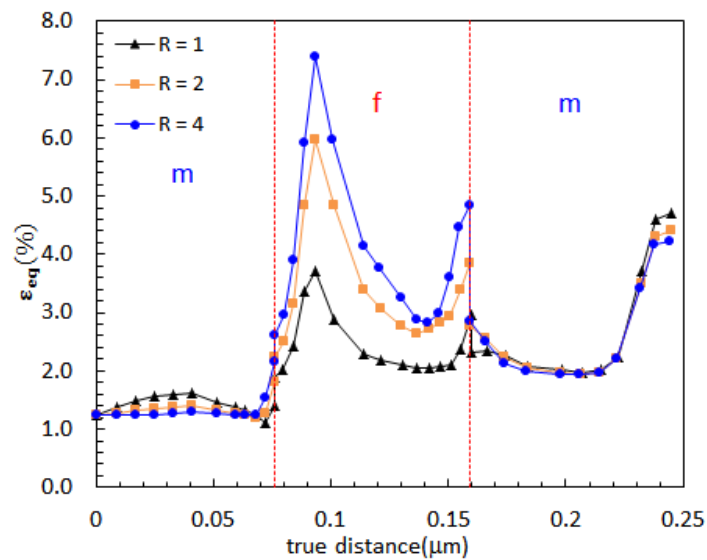


Figure 10: Isolated ferrite grain embedded within a martensite matrix (a) Path 2 used for variables outputs; (b) maximum principal stress variation along Path 2; (c) accumulated equivalent plastic strain (ϵ_{eq}) variation along Path 2. (The regions corresponding to ferrite and martensite grains are labelled 'm' and 'f', respectively).

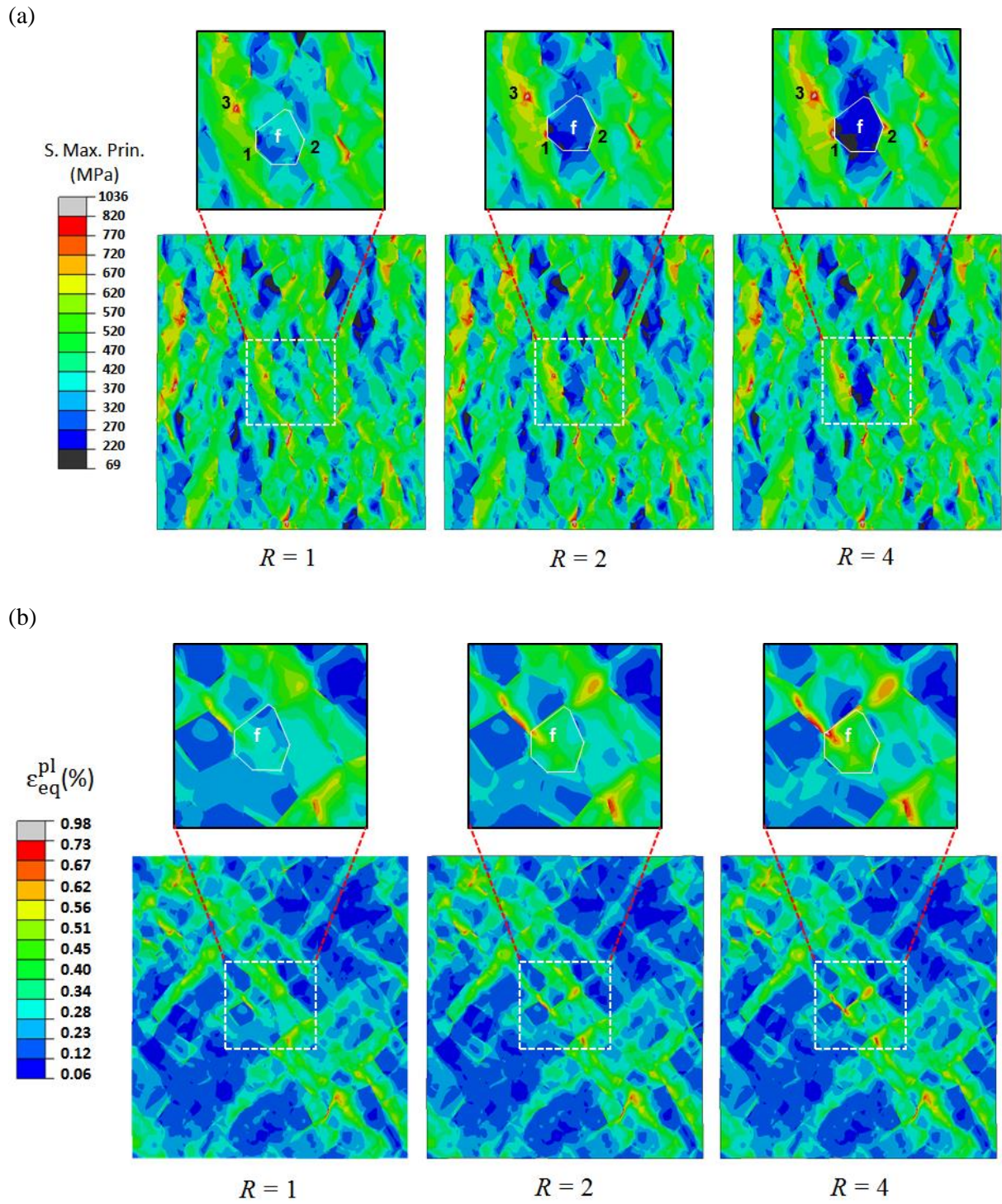


Figure 11: Predicted contour plots with single ferrite grain (a) maximum principal stress (b) accumulated equivalent plastic strain (ϵ_{eq}). The ferrite grain is labelled 'f' on the zoomed-in images

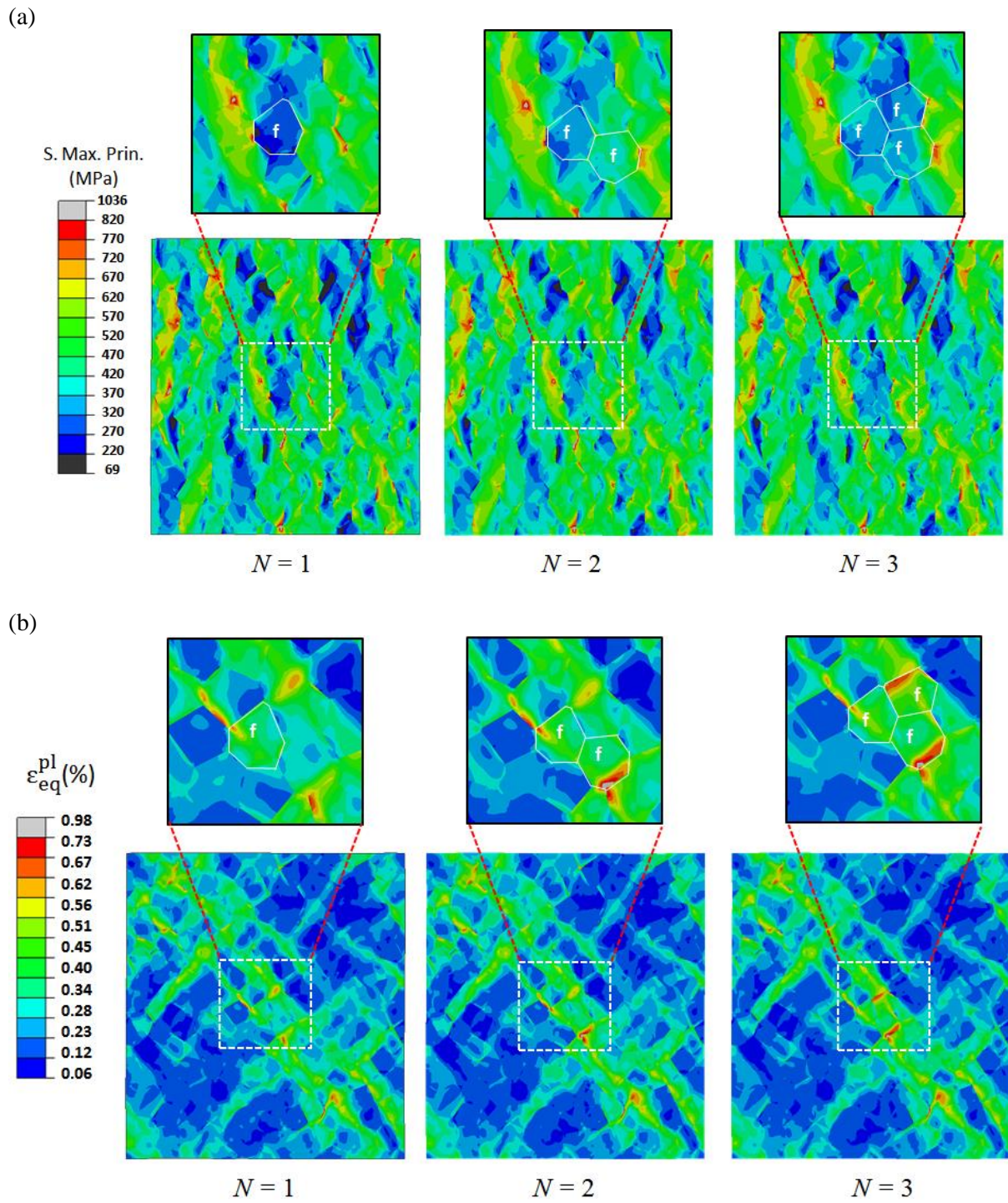


Figure 12: Predicted contour plots of ferrite aggregation case with $N = 1, 2, 3$, respectively ($R = 2$) (a) maximum principal stress (b) accumulated equivalent plastic strain (ϵ_{eq})

Tables

Table 1: Material constants used in the single crystal material model for IC-HAZ (martensite) at room temperature

Temperature	E (GPa)	ν	$\dot{\gamma}_0$ (s^{-1})	F (kJ/mol)	τ_0 (MPa)	S_0 (MPa)	S_{sat} (MPa)	h_s (MPa)	p	q
20°C	219	0.336	450	258	325	2.2	250	670	0.5	1.25